HHS Public Access

Author manuscript

Nat Struct Mol Biol. Author manuscript; available in PMC 2013 December 01.

Published in final edited form as:

Nat Struct Mol Biol. 2013 June ; 20(6): 662–670. doi:10.1038/nsmb.2564.

Substrate-specific structural rearrangements of human Dicer

David W. Taylor[1,2,14], **Enbo Ma**[3,14], **Hideki Shigematsu**[1,14], **Michael A. Cianfrocco**[4], **Cameron L. Noland**[3], **Kuniaki Nagayama**[5,6,7], **Eva Nogales**[2,3,8,9], **Jennifer A. Doudna**[2,3,9,10,11], and **Hong-Wei Wang**[1,12,13]

[1]Department of Molecular Biophysics and Biochemistry, Yale University School of Medicine, New Haven, CT, USA

[2]California Institute for Quantitative Biosciences, University of California, Berkeley, CA, USA

[3]Department of Molecular and Cell Biology, University of California, Berkeley, CA, USA

[4]Biophysics Graduate Group, University of California, Berkeley, CA, USA

[5]Division of Nano-Structure Physiology, Okazaki Institute for Integrative Bioscience, Okazaki, Japan

[6]National Institute for Physiological Sciences, National Institutes of Natural Sciences, Okazaki, Japan

[7]Department of Physiological Sciences, The Graduate University for Advanced Studies, Okazaki, Japan

[8]Life Sciences Division, Lawrence Berkeley National Laboratory, Berkeley, CA, USA

[9]Howard Hughes Medical Institute, University of California, Berkeley, CA, USA

[10]Department of Chemistry, University of California, Berkeley, CA, USA

[11]Physical Biosciences Division, Lawrence Berkeley National Laboratory, Berkeley, CA, USA

[12]Tsinghua-Peking Center for Life Sciences, Tsinghua University, Beijing, China

[13]Center for Structural Biology, School of Life Sciences, Tsinghua University, Beijing, China

Abstract

Dicer plays a central role in RNA interference pathways by cleaving double-stranded RNAs (dsRNAs) to produce small regulatory RNAs. Human Dicer can process long double-stranded and hairpin precursor RNAs to yield short interfering RNAs (siRNAs) or microRNAs (miRNAs), respectively. Previous studies have shown that pre-miRNAs are cleaved more rapidly than pre-

Correspondence should be addressed to H.W. (hongweiwang@tsinghua.edu.cn) and J.A.D. (doudna@berkeley.edu).

[14]These authors contributed equally to this work.

Author Contributions

D.W.T performed all electron microscopy and single particle analysis. E.M. performed protein and RNA purification. H.S. performed Zernike phase-contrast cryo-EM supervised by K.N. M.A.C. and E.N. assisted with focused classification. C.L.N. purified Dicer–PACT complex. D.W.T., J.A.D, and H.W. planned the experiments and wrote the manuscript. All authors analyzed and interpreted data and provided comments on the manuscript.

siRNAs *in vitro* and are the predominant natural Dicer substrates. We have used electron microscopy and single particle analysis of Dicer–RNA complexes to gain insight into the structural basis for human Dicer's substrate preference. Our studies show that Dicer traps pre-siRNAs in a non-productive conformation, while interactions of Dicer with pre-miRNAs and dsRNA binding proteins induce structural changes in the enzyme that enable productive substrate recognition in the central catalytic channel. These findings implicate RNA structure and cofactors in determining substrate recognition and processing efficiency by human Dicer.

Introduction

Dicer is a specialized, multi-domain RNase III enzyme that cleaves double-stranded RNA (dsRNA) precursors into ~21 base pair (bp) small RNA duplexes that guide gene regulation by RNAi-related pathways[1,2]. In addition to the two tandem catalytic (RNase III) domains, most metazoan Dicer proteins include an N-terminal DExH/D (ATPase–helicase) domain, a DUF283 domain, a PAZ domain, and a double-stranded RNA-binding domain (dsRBD) (Fig. 1a). During RNA processing, Dicer's PAZ domain recognizes the 5′ phosphate and the 2-nt 3′-overhang of a dsRNA substrate and positions the RNA for cleavage at a distance specified by the length between this domain and the intra-molecular RNase III heterodimer[3–5]. Dicer can recognize and cleave two major types of double-stranded RNAs. The enzyme processes hairpin RNA precursors to produce miRNAs, while it liberates siRNAs from long double-stranded substrates.

Although some organisms express two or more Dicer variants[6], human cells contain a single Dicer isoform. The majority of natural Dicer products in mammalian cells are miRNAs[7,8], although human Dicer is capable of processing both types of dsRNA substrates *in vitro*[9]. The enzyme cleaves pre-miRNAs at maximal rates two orders of magnitude higher than pre-siRNAs, and the autoinhibitory role of its N-terminal DExH/D domain in the processing of these perfect pre-siRNA duplexes has been established[9,10]. In humans, Dicer functions as a heterodimer with double-stranded RNA binding protein (dsRBP) partners, TRBP and PACT. These dsRBPs assist in RNA recruitment, positioning, and loading of products into RNA-induced silencing complexes[11–13]. Functional data support a role for the ATPase–helicase domain in recognizing dsRNA ends and terminal loops of hairpins in various eukaryotes[14–16]. However, the mechanism by which human Dicer distinguishes pre-miRNAs from pre-siRNAs and the role of the helicase domain in processing these substrates remains unclear.

An obstacle to understanding Dicer's mechanism is the lack of structural information. We and others have previously obtained three-dimensional (3D) reconstructions of human Dicer by negative stain electron microscopy (EM), revealing an L-shaped enzyme architecture with a flat platform density and a bi-lobed base-branch perpendicular to the platform[17,18]. We identified the base-branch in the structure as the N-terminal DExH/D domain of human Dicer by examining the structure of a DExH/D domain truncated mutant[18]. Recently, a revised topology for the enzyme has been proposed that reconciles previous Dicer models with some of its biochemical properties[19]. However, the mechanism of RNA recognition and binding by Dicer remains a major missing piece of structural information.

Because of their small size and dynamic nature, crystallography and conventional defocus-based phase contrast cryo-EM have had limited success in structural studies of Dicer–RNA complexes. To gain structural information on RNA recognition by Dicer, we have used Zernike-phase contrast cryo-EM[20–25] to obtain three-dimensional reconstructions of human Dicer bound both to a pre-siRNA and a pre-miRNA substrate. These structures, along with a quantitative single particle analysis of the conformational dynamics of the enzyme in response to substrates and dsRBP cofactors, support a structural model for small RNA precursor processing in humans. These results have important implications for our understanding of human Dicer's substrate selectivity and for how the activities of human Dicer relate to more specialized Dicers in other eukaryotes.

Results

Domain architecture of human Dicer

Previous structural studies of human Dicer have defined the overall L-shaped architecture of the enzyme[17,18]. To unambiguously determine the overall topology of the protein and identify specific domains, we performed single particle EM analysis of human Dicer in complex with antibodies recognizing specific regions of the enzyme. Reference free two-dimensional (2D) alignment and classification of the human Dicer–antibody complexes produced two distinct types of class averages: one in which a single Dicer molecule is bound to a single antibody, and a second in which two Dicer molecules are tethered by a single antibody. Both types of averages revealed clear and consistent locations of antibody binding (Fig. 1b and Supplementary Fig. 1a,b). We found that antibody mAb 77, which recognizes an epitope in the C-terminal RNase IIIa and IIIb domains[26], labeled the hinge region between the base-branch and the platform (Fig. 1b), while antibody mAb 83, which recognizes Dicer's PAZ and DUF283 domains[26], labeled the cap of the platform (Fig. 1b). In agreement with our previous results, an antibody that binds to the N-terminal His_6-tag specifically labeled the tip of human Dicer's base-branch (data not shown)[18]. These results suggest an overall topology for the protein in which the polypeptide chain folds back on itself, bringing the N- and C-termini into close proximity. Our results using antibody-guided localization of domains in the native enzyme agree with the topology recently proposed using engineered Dicer proteins[19].

Cryo-EM structure of human Dicer

In order to visualize RNA binding to Dicer using electron microscopy, we examined the frozen-hydrated enzyme by cryo-EM. Unfortunately, individual human Dicer particles observed by conventional cryo-EM could not be easily identified because of their small size (~220 kDa) (Supplementary Fig. 2a). We turned to the recently developed electron microscopy technique called Zernike phase contrast cryo-electron microscopy (ZPC-cryoEM) to obtain 3D structures of Dicer and Dicer–RNA complexes. This method utilizes a thin carbon-film with a small hole in the center (a phase-plate) that is inserted in the back focal plane of the objective lens of the microscope to retard the phase of scattered electrons by $\pi/2$. This changes the contrast transfer function (CTF) from a sine to a cosine function[20] and provides higher contrast for ice-embedded specimens and the detection of macromolecules with sizes as small as 100 kDa[27].

Using ZPC-cryoEM, we observed ice-embedded Dicer molecules with one order of magnitude higher contrast than conventional cryo-EM and could easily identify single particles in raw micrographs (Supplementary Fig. 2b). After high-pass filtering the micrographs taken with the phase-plate using a modulating function (Supplementary Note and Supplementary Fig. 2c–e), we used conventional single particle reconstruction methods to obtain a 3D reconstruction of human Dicer at ~26 Å resolution from 4,800 particle images (based on the 0.5 Fourier Shell Correlation (FSC) criterion) (Fig. 1c, Supplementary Fig. 3a–c). The cryo-EM reconstruction of human Dicer matches the overall molecular architecture of our previous negative stain reconstruction. Guided by the antibody-labeling results, we were able to dock the atomic models of *Giardia intestinalis* Dicer (PDB 2QVW[28]) into the platform, with the PAZ anchored in the larger lobe of the cap, and a PHYRE[29] homology model of human Dicer's DExH/D domain based on human RIG-I (PDB 2YKG[30]) into the base-branch of the reconstruction (Fig. 1c).

Cryo-EM structures of human Dicer–RNA complexes

In vitro dicing assays have shown that human Dicer processes a 35 bp pre-siRNA (37ab) with maximal cleavage rates (k_{cat}/K_m) that are two orders of magnitude slower than those measured for a pre-miRNA (pre-let-7), although the binding affinities for the RNA substrates are similar[10]. This suggests that the two precursors interact with the protein differently or that substrate-specific conformational rearrangements account for the selectivity of the enzyme. To determine the structural basis for substrate-specific processing rate differences, we performed ZPC-cryoEM of human Dicer bound to either 37ab or pre-let7, in a buffer containing EDTA in order to retain binding while inhibiting the processing of the RNA. Raw micrographs of Dicer in complex with RNA contained particles with similar contrast to those of apo-Dicer. Using the 3D density of apo-human Dicer low-pass filtered at 80 Å resolution as an initial model, we performed 3D maximum likelihood heterogeneity analysis[31] of human Dicer in complex with 37ab and pre-let7, respectively. For each human Dicer–RNA complex, one subgroup of particles showed clear additional density in the resulting reconstruction and was further refined (Supplementary Fig. 3d). Using these methods, we obtained cryo-EM reconstructions of human Dicer in complex with 37ab and pre-let7 at 29 Å and 31 Å resolution (0.5 FSC criterion) from 6,200 and 4,100 particles, respectively (Fig. 2a,b and Supplementary Fig. 3a,e–h).

The reconstruction of human Dicer–37ab showed a prominent additional rod-shaped density extending from the cap to the base-branch of the enzyme (Fig. 2a). There is a relative rotation between the cap and platform regions of human Dicer, possibly induced by the bound RNA, causing the PAZ domain to pivot down towards the platform of the enzyme (Supplementary Fig. 3i). To model the interaction between Dicer and a pre-siRNA, we docked the major domains of Dicer and a 35 bp A-form RNA duplex representing 37ab into the reconstruction. The additional rod-shaped density can easily accommodate the RNA duplex. The arrangement of human Dicer's PAZ and DExH/D domains traps the dsRNA ~30 Å outside of the platform region. Effectively, these domains hold the dsRNA in a non-catalytically competent state away from the RNase III active sites of the enzyme. This architecture provides a structural explanation for the autoinhibitory role of the DExH/D domain in the processing of this substrate.

In contrast, the cryo-EM reconstruction of human Dicer–pre-let7 showed an additional globular density (Fig. 2b) connected to human Dicer's platform near the end closest to the base-branch. This is the same region that was labeled by the antibody mAb 77, which recognizes an epitope near the RNase IIIa and IIIb domains. Binding of this RNA is accompanied by an outward bending of the branch away from the platform, exposing the pre-let7 binding site (Supplementary Fig. 3j). There is also a smaller rotation of the cap relative to the platform of human Dicer. Based on our cryo-EM structures of both Dicer–RNA complexes, the two major precursors of human Dicer bind to the enzyme in a substrate-specific manner.

Substrate-specific conformational dynamics of human Dicer

We hypothesized that pre-let7, unlike the pre-siRNA, may induce a conformational change in human Dicer that accounts for its access to the platform region in our 3D structure and for the preferential dicing activity observed *in vitro*. We further investigated the conformational dynamics of human Dicer in the presence of pre-let7 and 37ab using negative stain EM and focused 2D classification, as previously described[32,33]. All samples were prepared on ice to ensure we were not observing structural changes as a result of dicing activity. We performed reference-free 2D alignment and classification for apo-Dicer and both of the human Dicer–RNA complexes (Supplementary Fig. 4 and **Online Methods**). Approximately 50% of the class averages from each independent set of particles showed the characteristic L-shaped view of human Dicer, in which the cap has a triangular shape and the platform has a large elliptical density with a small knob at the end, closest to the connection to the branch (Supplementary Fig 4a,b). For the apo-Dicer particles, a majority of the class averages in the L-shaped view showed the canonical positioning of the branch and platform roughly perpendicular to one another, as previously observed[17–19] (Supplementary Fig. 4a). Interestingly, while some of the class averages in the Dicer–RNA complexes showed the canonical perpendicular arrangement of the platform and base-branch, many class averages showed a wide distribution of angles between them (Supplementary Fig. 4b).

We performed a rigorous 2D focused classification procedure on this preferred, well-characterized view of the enzyme in order to quantitatively describe the heterogeneity present in each of the samples. For each particle stack, we aligned all of the particles corresponding to the L-view to the rigid platform and cap density (Supplementary Fig. 4c,d). Classifying the aligned particles based on a mask encompassing the possible positions of the branch, we obtained class averages of the enzyme with clear features for both the rigid core and base-branch (Supplementary Fig. 4e,f). We used ten-square-pixel boxes to place a marker in the middle of the cap, the circular bulge at bottom of the platform, and the tip of the base-branch in each class average, then used the center of these boxes as coordinates A, B, and C, respectively, for distance measurements between domains (Fig. 3a, **inset** and Supplementary Fig. 4g). AB (platform length) within the rigid core consisting of the platform and cap was measured to be between 106 and 110 Å for each dataset analyzed, with a standard deviation of ~5 Å (Supplementary Fig. 4h–j). This suggests that the cap and platform of the enzyme do not change in response to substrate and, because the pixel size is 4.36 Å, demonstrates the accuracy of our measurements to within ~1 pixel.

To calculate class averages of certain conformations of the enzyme, we summed particle images within a defined range of AC and BC distances describing the position of the mobile branch domain relative to the rigid platform and cap, AC (cap–branch distance) and BC (branch length). Using this method, in addition to the characteristic L-shaped conformation of Dicer, we visualized four populated states with the base-branch bending away from or towards the platform, with either an extended or contracted branch (Fig. 3a). We plotted the 2D distributions of branch length (BC) vs. cap–branch distance (AC) for apo-Dicer and each Dicer–RNA complex, where each point represented the measurements of a specific class average (Fig. 3b–d). Along with these plots, we calculated histograms of the frequency of cap–branch distance and branch length by projecting the 2D distributions along each of the respective axes. Additionally, we calculated the percentage of particles displaying cap–branch distances of ≤ 85, 86–120, and > 120 Å, which we refer to as the closed, canonical and open states of the enzyme, respectively (Table 1). The apo-Dicer particles are tightly clustered around distances of ~100 Å for both cap–branch distance (95%) and branch length (Fig. 3b), corresponding to the canonical conformation. Interestingly, the Dicer–RNA complexes showed significant deviations from the tightly clustered distribution of apo-Dicer in opposite directions for each substrate (see Supplementary Tables 1 and 2 for data statistics and significance tests, respectively). The more efficiently cleavable substrate, pre-let7, induced more conformers (46%) in which the base-branch bends away from the platform (cap–branch distance of ~130–140 Å) or an opening of the enzyme, coupled to an extension of the branch itself (branch length of ≥ 110 Å) (Fig. 3c). In contrast, the less efficiently cleavable duplex substrate, 37ab, showed a subpopulation of particles (40%) with an inward bending of the branch toward the platform (cap–branch distance of ~60–80 Å) or a closing of the enzyme, coupled with compaction of the branch (branch length of ≤ 100 Å) (Fig. 3d). For the Dicer–37ab complex, there is also a minor subpopulation of particles (27%) that exhibited the ‘open’ state of the enzyme, resembling the preferred conformation in Dicer–pre-let7.

Changes in cap–branch distance (AC) describe a pivoting of the base-branch toward or away from the platform because this movement reflects an in-plane rotation of the domain (verified by 3D random conical tilt reconstruction described below); however, we cannot rule out the possibility that changes in branch length (BC) describe an out-of-plane rotation as opposed to an extension or contraction of the domain itself. In either case, changes in the branch length still reflect unique states of the branch with respect to the core of the enzyme. Since human Dicer is purified using established protocols[34] and the same preparation was used between a majority of the focused classification experiments, these conformational changes are most likely due to the presence of the RNA substrates, as any underlying biochemical heterogeneity would be constant.

Dicer’s pre-miRNA substrates are diverse and can differ drastically in hairpin loop size, loop structure, and extent of complementarity in the stem. We predicted that the opening of human Dicer that we observed in the presence of pre-let7 was a result of the enzyme recognizing the terminal loop of this pre-miRNA. To test this hypothesis, we extended our conformational analysis to a second pre-miRNA substrate, zebrafish pre-miR-430[35]. While pre-let7 has a fairly large single-stranded terminal loop (~27 nts) (Supplementary Fig. 5a), pre-miR-430 has a smaller terminal loop (~19 nts) and fewer mismatched base pairs in the

stem (Supplementary Fig. 5b). Consistent with our hypothesis, pre-miR-430 induced a majority of Dicer particles (70%) into the open state of the enzyme in which the base-branch bends away from the platform (Fig. 4a and Supplementary Fig. 5c). If the open conformation we observed for Dicer in complex with both pre-miRNAs reflects the catalytically competent or more productive form of the enzyme, then pre-miR-430 should be processed at rates comparable to pre-let7 and substantially higher than the dsRNA 37ab. In agreement with this line of reasoning, Dicer cleavage assays showed that both pre-miRNAs were processed similarly at higher rates than 37ab (Fig. 4b). Thus, the presence of the terminal loop within pre-miRNA substrates stabilizes the open conformation of Dicer and this opening of the enzyme is correlated with increased rates of cleavage *in vitro*.

dsRBP-sampled conformational states of human Dicer

Based on our focused classification analysis of apo-Dicer and Dicer–RNA complexes, the helicase domain changes its position relative to the rigid core of Dicer in response to RNA substrates, resulting in changes in the overall architecture of the enzyme. These findings suggest that the helicase domain is the primary sensor of RNA, and that its conformation within Dicer selectively favors productive binding to particular types of substrates. In humans, Dicer functions in complex with the double-stranded RNA binding proteins (dsRBPs) TRBP and PACT in its interactions with small RNA precursors. Previous biochemical and structural studies have indicated that these dsRBPs bind to the DExH/D domain or base-branch of human Dicer[18,36]. Because the branch is also the domain that is sensing RNA precursors, we hypothesized that dsRBPs may influence RNA binding and dicing activity by promoting productive conformations of the enzyme. Using the same 2D focused classification approach, we analyzed the structural dynamics of reconstituted Dicer–TRBP and Dicer–PACT complexes. Interestingly, the distribution of branch length vs. cap–branch distance for the Dicer–TRBP complex closely resembled Dicer–37ab, particularly in cap–branch distance (Fig. 5a and Supplementary Fig. 5d). There is a major subpopulation of particles (30%) exhibiting the closed conformation only seen in Dicer–37ab where the branch bends inward toward the platform with contraction of the branch.

The human Dicer–TRBP heterodimer cleaves 37ab at rates 500% higher than Dicer alone[10]. Because the binding affinities of human Dicer and human Dicer–TRBP to this substrate are similar[9], we hypothesized that the enhanced cleavage activity may be the result of TRBP facilitating conformational changes in human Dicer upon RNA binding for productive substrate loading. If this productive loading event is occurring, we predicted that the Dicer–TRBP–37ab particles would selectively favor the open conformation observed for both Dicer–pre-miRNA particles. Indeed, the distribution of branch length vs. cap–branch distance showed a dramatic shift away from both Dicer–TRBP and Dicer–37ab distributions towards Dicer–pre-let7 and Dicer–pre-miR-430 distributions (Fig. 5b and Supplementary Fig. 5e), with an overwhelming number of particles (85%) showing a bending of the base-branch away from the platform or an opening of the enzyme. Since the Dicer–TRBP heterodimer alone and Dicer–37ab both exhibit the closed conformation of the enzyme, it is possible that this state is an on-pathway loading intermediate.

In contrast to Dicer–TRBP, the biochemical properties of Dicer–PACT are poorly understood. The distribution of branch length vs. cap–branch distances for the Dicer–PACT complex showed two subpopulations of particles matching states observed in both Dicer–37ab and Dicer–pre-let7 (Fig. 5c and Supplementary Fig. 5f,g). There is a major class of particles exhibiting a rotation of the base-branch away from the platform or open state (35%) with an extension of the branch, similar to the preferred conformation of Dicer–pre-let7. There is also a minor class of particles that resembled the closed conformation (16%) only seen in Dicer–37ab where the branch bends inward toward the platform with contraction of the branch. These results suggest both dsRBPs play a role in rearranging the enzyme and suggest the involvement of PACT in Dicer processing of small RNA precursors.

Because the Dicer–PACT complex exhibited the three major states observed within our 2D analysis of apo-Dicer and Dicer–RNA complexes, we performed 3D reconstructions of these three states using the random conical tilt[37] (RCT) methodology. Using reference-free 2D class averages matching unique subpopulations of particles in Dicer–pre-let7, apo-Dicer, and Dicer–37ab (Fig. 6a–c), we obtained RCT models of the open, canonical, and closed states of the enzyme (Supplementary Fig. 6a–d). Using multi-model projection matching refinement, we determined the 3D structures of these conformers at ~26 Å resolution (based on the 0.5 FSC criterion) (Supplementary Fig. 6e–g). While the branch adopted different conformations with respect to the rest of the enzyme in all three reconstructions (Fig. 6a–c), the platform and cap of the enzyme remain mostly unchanged (Fig. 6a–c). This result confirms that the helicase domain, or base-branch, is the component of the enzyme changing in response to RNA substrates and protein binding partners. Importantly, all of the RCT reconstructions of negatively stained apo-Dicer particles exhibited the canonical orientation of the branch (Supplementary Fig. 7a,b). The RCT analysis strongly supports the argument that the different 2D states reflect unique 3D structures present within our samples.

Discussion

Cryo-EM structures of Dicer–RNA complexes indicate that Dicer employs distinct recognition modes for pre-miRNA and pre-siRNA substrates, both involving capture by the N-terminal helicase domain. A quantitative analysis of human Dicer conformational dynamics show that binding of small RNA precursors and the presence of dsRBP partners confer substrate and cofactor-specific rearrangements of the helicase domain, while the cap and platform core of the enzyme remains unchanged. These results suggest the N-terminal ATPase–helicase domain acts as the primary RNA sensor for discriminating between the dsRNA molecules that the enzyme encounters in the cell and provides the structural basis for human Dicer's substrate specificity (Fig. 7).

Based on our antibody labeling results, the catalytic RNase IIIa and IIIb domains are positioned in the platform of human Dicer directly under the base-branch, which we previously determined is the N-terminal DExH/D domain, while the PAZ-DUF283 domains are in the cap at the other end of the platform. The reconstructions of human Dicer–pre-let7 and Dicer–37ab indicate that the DExH/D domain is responsible for constraining one end of the RNA substrate. In the case of Dicer–37ab, the pre-siRNA is held between the helicase

and PAZ domains, away from the enzyme's catalytic core. In contrast, the additional density in the Dicer–pre-let7 reconstruction, attributed to pre-let7 RNA, is near the catalytic platform of the enzyme and thus ready for processing, while also interacting with the base-branch. The bending of the base-branch away from the platform observed in our Dicer–pre-let7 reconstruction may allow the pre-let7 substrate to gain access to the RNase IIIa and IIIb sites that are otherwise sterically occluded. Based on our two substrate-bound structures, a dsRNA precursor ≥ 30 bp in length would be wedged between the PAZ domain and the DExH/D domain and therefore would not be cleaved efficiently by the enzyme. This mirrors a previous study that found duplexes of >27 bp to be poor Dicer substrates[38].

Compared to a pre-siRNA, a pre-miRNA's distinct features include mismatches in the stem region and a loop opposite the terminal end of the stem. This combination of features could allow for miRNA precursors to evade inhibition by the helicase domain. Specifically, the terminal single-stranded loop of pre-miRNAs might interact with the helicase domain along a different surface or by a different mode than the helical ends of siRNA precursors. In agreement with this hypothesis, inserting a mismatch within a perfectly matched stem does not abrogate the inhibitory effect of the DExH/D domain[16]. However, placing a terminal loop at the end of a perfectly matched stem allows the precursor to escape the inhibition from the DExH/D domain and favors cleavage rates comparable to pre-let7[16]. Alternatively, pre-miRNAs may evade this inhibition by folding into complex tertiary structures or by taking advantage of a flexible terminal loop for access to the platform. In agreement with the former, recent studies suggest that the terminal loop of primary-let7, the precursor of pre-let7, is structured[39–41]. It is possible that the compact, globular density attributed to pre-let7 in our cryo-EM reconstruction is the structured terminal loop of this pre-miRNA.

Dicer binding to 37ab and pre-let7 populates conformations of the enzyme that are closed and opened, respectively. Because the branch is reorganized in response to RNA precursors, the helicase domain of human Dicer is most likely the primary sensor of RNA for the enzyme, and the effect of its position on the architecture of Dicer selectively promotes binding of certain RNA substrates. We hypothesize that the opening of the base-branch of human Dicer in complex with pre-let7 and pre-miR-430 might be the catalytically competent state of the enzyme. This state could be induced by the interaction of the pre-miRNA's terminal loop with the DExH/D domain. Our cryo-EM reconstruction of Dicer–pre-let7 shows both the additional density for pre-let7 along the platform and an outward bending of the branch. Additionally, a recent study showed that human Dicer uses a loop-counting rule *in vivo*[42]. It is possible that human Dicer's helicase domain recognizes the loop and is the actual sensor in this counting mechanism through the domain reorganization we observed. The closed state of the enzyme observed in a subpopulation of Dicer bound to the pre-siRNA most likely represents the auto-inhibited state of the enzyme or an RNA-loading intermediate.

The Dicer–TRBP complex exhibits a subpopulation of particles in the closed conformation unique to Dicer–37ab complexes. Conversely, the tripartite Dicer–TRBP–37ab complex shifts the distribution of cap–branch distances into the open conformation, similar to the state observed for Dicer in the presence of either pre-miRNA substrate. This suggests that TRBP is important for correctly loading the dsRNA substrate for productive processing. The

Dicer–PACT complex straddles the conformational space observed for both Dicer–pre-miRNA complexes. The association of PACT with Dicer may arrange and poise the enzyme for successful RNA binding, loading, or processing. The 3D model of the closed state clearly shows the branch in a position to exclude RNA binding from the platform or the catalytic core of the enzyme. On the other hand, the 3D model of the open state of the enzyme shows the base-branch bent away from the platform, enabling this channel to accommodate RNA substrates.

Several studies have shown that *Drosophila* Dicer-1 and Dicer-2 employ distinct strategies for discriminating and processing their respective substrates[15,43]. While human Dicer is a non-processive, ATP-independent enzyme on long dsRNA[44], if the molecular architecture of Dicer-2 is conserved as reported[19], the state we observed could be similar to the altered reaction mode proposed for Dicer-2 in processing dsRNA[14,43]. The ATPase–helicase domain may clamp around the RNA precursor for repositioning Dicer along long dsRNA during processive cleavage by the enzyme. Our cryo-EM structure of Dicer bound to pre-let7 shows that this RNA adopts a conformation remarkably different from an A-form RNA duplex for productive enzyme–substrate complex formation, similar to the mechanism reported for specific recognition of pre-miRNA structural features by Dicer-1[15]. We hypothesize that human Dicer utilizes similar strategies to both Dicer-1 and Dicer-2 for recognition and processing of both types of substrates. Additionally, other studies have demonstrated evolutionary conservation of a short ~42-nt pre-miRNA, which bypasses Dicer for processing by Argonaute2[45,46]. Our results suggest that there are other evolutionary pressures on pre-miRNA structure. It is tempting to hypothesize that certain Dicer-dependent pre-miRNA hairpins have evolved distinctive structures to favor interaction and processing by Dicer, perhaps to rapidly increase levels of mature miRNAs for system robustness or for important developmental transitions.

Accession Codes

The structures of human Dicer, Dicer–37ab, and Dicer–pre-let7 have been deposited into the EMDataBank with accession codes EMD-5601, EMD-5602, and EMD-5603, respectively. The structures of human Dicer–PACT in the closed, canonical, and open conformation have been deposited into the EMDataBank with accession codes EMD-5604, EMD-5605, and EMD-5606, respectively.

Online Methods

Negative stain EM sample preparation and data collection

We diluted hDicer, hDicer–RNA, hDicer–antibody samples for negative stain EM to a concentration of ~50 nM in 20 mM HEPES, pH 7.5, 150 mM KCl, 3 mM EDTA, 1 mM DTT, and 2.5% glycerol immediately before applying the sample to glow-discharged holey carbon grids with a thin layer of carbon over the holes. After adsorption for 1 min, we stained the samples consecutively with three droplets of 2% (w/v) uranyl formate solution, blotted off the residual stain and air-dried the sample in a hood. We examined the specimens using an FEI Tecnai-12 electron microscope equipped with a LaB6 filament and operated at 120 kV acceleration voltage, using a nominal magnification of 42,000. We recorded images

on a 4k x 4k CCD camera (Gatan) with a pixel size of 2.6 Å, using low-dose mode with an exposure dose of 20–30 $e^{-}Å^{-2}$. The defocus used to collect images was −0.8 μm to −1.1 μm.

2D analysis of Dicer–antibody complexes

We performed semi-automatic particle picking using EMAN[47] to box particles from the raw micrographs into boxes of 158 × 158 and 170 × 170 square pixels for mAb 77 and mAb 83-labeled Dicer complexes, respectively. The particles were high-pass and low-pass filtered and normalized prior to analysis. 1,500–2,000 raw particles of each Dicer–antibody complex were subjected to reference-free alignment and classification using multivariate statistical analysis and multi-reference alignment in IMAGIC[48] to a total of 60–100 classes (~20 particles per class).

ZPC-cryoEM sample preparation and data collection

We diluted hDicer and hDicer–RNA complexes for cryo-EM to a concentration of ~200 nM in 20 mM HEPES, pH 7.5, 150 mM KCl, 3 mM EDTA, 1 mM DTT, and 2.5% glycerol immediately before applying the sample to glow-discharged Quantifoil R 1.2/1.3 MO 200 mesh holey carbon grids. The samples were automatically blotted for 4–5 s at −2.5 mm offset in 100% humidity at 22°C and flash frozen into liquid ethane using an FEI Vitrobot. Ice thickness of the sample ranged from 50–120 nm using this method. Grids were examined with a JEM-3100FFC (JEOL) cryo-EM. The microscope was equipped with a field emission gun and an in-column (omega-type) energy filter. The microscope was operated at 300 kV acceleration voltage, with in-focus Zernike phase contrast imaging condition[27]. The specimen temperature was maintained at ~55 K, as described for JEM-3100FFC[27]. The Zernike phase plate, inserted at the back focal plane of the objective lens, was made of a vacuum-evaporated amorphous carbon film with a thickness of ~27 nm, optimized for 300 kV electrons. The central hole in the phase plate was 0.5 μm in diameter, corresponding to a 25 nm frequency cutoff in the image. The phase plate was continuously maintained above 200°C in order to prevent beam-induced contamination[49]. Data was collected at a detector magnification of 100,000, using zero-loss energy filtering with a 20 $e^{-}V$ slit width, and an incident electron dose of 20 $e^{-}/Å^{-2}$. Images were recorded on a 2k x 2k CCD camera (Megascan 795, Gatan) with a pixel size of 3.07 Å. Data acquisition was performed with a minimum dose system implemented by the manufacturer and using special developed software that communicates with the TEM-controller (JEOL) to include alignment of the phase plate in the sequence[22].

Cryo-EM reconstructions

Particles in the filtered micrographs (described in the Supplementary Note) were boxed semi-automatically using the boxer program in EMAN[47]. Briefly, particles were selected using the raw ZPC-cryoEM micrographs and these coordinates were used for extracting the particles from the corresponding filtered micrographs. We accumulated 6,000, 24,000, and 12,000 particles from ZPC-cryoEM micrographs of apo-Dicer, Dicer–37ab, and Dicer–pre-let7 specimens, respectively. For the reconstructions of apo-Dicer and Dicer in complex with its RNA substrate, we used standard projection matching refinement of raw particles in SPIDER[50] against our previous 3D reconstruction of human Dicer obtained by negative stain EM low-pass filtered to 80 Å as the initial model.

Maximum-likelihood 3D analysis[31] was performed on apo-Dicer and the Dicer–RNA complexes to reveal any conformational heterogeneity among the particles. Briefly, each dataset was first aligned to the low-pass filtered model obtained from the projection matching refinement to correct normalization errors and an arbitrary number of seed models (3 or 4 to maintain a reasonable number of particles within each subgroup) from randomly generated subgroups of each dataset were reconstructed for further analysis. We then used the ML3D[31] function in the Xmipp software package[51] to reconstruct the 3D models of each sample using an iterative maximum-likelihood reconstruction algorithm. While heterogeneity was not apparent in the apo-Dicer dataset, we observed striking differences among the models for both Dicer–RNA complexes, i.e. the presence or absence of an additional density in the models. Among these, the subpopulation of particles with the most prominent additional density was used for projection matching refinement against the corresponding ML3D output model in Xmipp[51]. This combination of heterogeneity analysis and projection matching refinement led to the final reconstruction of human Dicer–37ab.

For the Dicer–pre-let7 reconstruction, we were able to improve the model using multi-model refinement with EMAN2/SPARX[52,53] software libraries for iterative projection matching refinement as described[54] using the three final Dicer–PACT conformers as initial models. The model with the clearest features after refinement showed both an additional density and an outward bending of the helicase domain away from the platform. This model had excellent agreement between its reprojections and reference-free class averages and served as our final reconstruction of Dicer–pre-let7. The three-dimensional maximum-likelihood refinement reconstructions of Dicer–37ab and Dicer–pre-let7, respectively, have been validated using several conventional single particle methods currently employed in the field (FSC curves, Euler angle distribution, and matching reference-free 2D class averages to reprojections of the structure) (Supplementary Fig. 3). The reconstruction presented for each of the RNA-bound Dicer complexes comes from the map with both the largest subgroup of particles being sorted into the resulting structure and clear additional density for the RNA substrate. We ran the maximum-likelihood reconstruction algorithm at least three times for each Dicer–RNA complex with identical results. More importantly, we used several starting models for the creation of the initial seeds of the refinement procedure and obtained reconstructions with similar features and placement of additional density for the RNA-bound enzyme.

Focused 2D classification of Dicer complexes

In order to study the effect of RNA on the structure of Dicer, we used a focused classification scheme for two-dimensional alignment and classification of the particles (Supplementary Fig. 4). First, we used semi-automated particle picking in EMAN[47] to collect between 4,000 and 10,000 individual particle images for each sample. All of the individual particle stacks from each dataset were subjected to iterative reference-free two-dimensional alignment and classification using a neural network classification approach[55] and multi-reference alignment[48] (MRA) to a final number of ~200 classes (Supplementary Fig. 4a,b). We focused the remainder of the analysis on particles extracted from classes that showed Dicer in the characteristic L-shape view. These particles were aligned to the rigid platform-cap core (Supplementary Fig. 4c) using M-R-A program in IMAGIC[48]. We then

performed multivariate statistical analysis (MSA) in IMAGIC within a mask around the large region delimited by sites populated by the mobile helicase domain. Eigen-images showed the conformational flexibility in this region (Supplementary Fig. 4e). Hierarchical ascendant classification was used to group the particles into classes of ~20 particles per class (Supplementary Fig. 4f).

Boxes of 10 square pixels were placed on the class averages in the middle of the cap, the knob at the end of the platform, and the center of the tip of the base-branch using BOXER in EMAN[47]. The centers of these boxes were used as points A, B, and C, respectively, for calculating AC (cap–branch distance), BC (branch length), and AB (platform length) using the distance formula (Supplementary Fig. 4g). BC vs. AC distances were plotted for each sample using MATLAB (MathWorks, Inc.). Histograms of BC and AC distances along the axes were constructed by binning the distances into 10 Å intervals using MATLAB and fitted using a maximum-likelihood estimation of a mixed Gaussian distribution (‘gmdistribution.fit’).

Random conical tilt (RCT) reconstruction of Dicer–PACT

Tilt-pairs of micrographs were recorded manually at 0° and 60°, respectively, as described above (Supplementary Fig. 6a). For the three-dimensional reconstructions of conformers in our focused 2D classification of Dicer complexes, we generated *ab initio* models using the random conical tilt method (RCT)[37] with the RCT module[56] in the Appion image-processing pipeline[57]. Particles were correlated between tilt-pairs automatically using TiltPicker[58], binned by 2, and extracted from raw micrographs. The untilted particle images were subjected to iterative maximum-likelihood two-dimensional classification and averaging using the ml2d[59] command in Xmipp[51] and RCT volumes were calculated for each class average using back-projection in SPIDER[50] based on the angles and shifts used in aligning untilted particles and the angle between tilt-pairs. These RCT models were low-pass filtered and subjected to multi-model iterative projection matching refinement using the untilted particle images as previously described[54] with libraries from EMAN2 and SPARX software packages[52,53] (Supplementary Fig. 6b–g).

Supplementary Material

Refer to Web version on PubMed Central for supplementary material.

Acknowledgments

We thank W. Filipowicz (Friedrich Miescher Institute for Biomedical Research, Basel, Switzerland) for human Dicer antibodies; A. Giraldez (Department of Genetics, Yale University School of Medicine, New Haven, CT, USA) for purified pre-miR-430; G. Lander, P. Grob, and T. Houweling for expert EM and image-processing assistance; A. Brewster for help with creating the homology model of human dicer; T. Albergo for help with particle picking; members of the Wang, Doudna, Nagayama, and Nogales labs for helpful discussions; A. Giraldez, D. Cifuentes, A. Bazzini, S. Baserga, J. Steitz, and members of the Giraldez and Baserga labs for discussion and expert technical assistance; H. Okawara and M. Ohara (Division of Nano-Structure Physiology, Okazaki Institute for Integrative Bioscience, Okazaki, Japan) for preparing the Zernike phase plates; the Yale Center for Cellular and Molecular Imaging (CCMI) and Yale Center for High Performance Computation in Biology and Medicine; D.W.T is a US National Science Foundation (NSF) Graduate Research Fellow and a NSF/Japan Society for the Promotion of Science East Asia and Pacific Summer Institute Fellow. This work was supported in part by US National Institutes of Health (NIH) molecular biophysics training grant 5 T32 GM008283 (D.W.T.), the Core Research for Evolutional Science and Technology (CREST) of Japan Science and Technology Agency (K.N.), NIH

5R01GM073794 (J.A.D.), the Human Frontiers in Science Program RPG0039/2008-C (E.N.), Smith Family Awards Program for Excellence in Biomedical Research (H.W.), and National Natural Science Foundation of China 31270765 (H.W.). J.A.D and E.N. are Howard Hughes Medical Institute Investigators.

References

1. Bernstein E, Caudy AA, Hammond SM, Hannon GJ. Role for a bidentate ribonuclease in the initiation step of RNA interference. Nature. 2001; 409:363–6. [PubMed: 11201747]
2. Carmell MA, Hannon GJ. RNase III enzymes and the initiation of gene silencing. Nat Struct Mol Biol. 2004; 11:214–8. [PubMed: 14983173]
3. Macrae IJ, et al. Structural basis for double-stranded RNA processing by Dicer. Science. 2006; 311:195–8. [PubMed: 16410517]
4. MacRae IJ, Zhou K, Doudna JA. Structural determinants of RNA recognition and cleavage by Dicer. Nat Struct Mol Biol. 2007; 14:934–40. [PubMed: 17873886]
5. Park JE, et al. Dicer recognizes the 5′ end of RNA for efficient and accurate processing. Nature. 2011; 475:201–5. [PubMed: 21753850]
6. Tomari Y, Zamore PD. Perspective: machines for RNAi. Genes Dev. 2005; 19:517–29. [PubMed: 15741316]
7. Calabrese JM, Seila AC, Yeo GW, Sharp PA. RNA sequence analysis defines Dicer's role in mouse embryonic stem cells. Proc Natl Acad Sci U S A. 2007; 104:18097–102. [PubMed: 17989215]
8. Chiang HR, et al. Mammalian microRNAs: experimental evaluation of novel and previously annotated genes. Genes Dev. 2010; 24:992–1009. [PubMed: 20413612]
9. Ma E, MacRae IJ, Kirsch JF, Doudna JA. Autoinhibition of human dicer by its internal helicase domain. J Mol Biol. 2008; 380:237–43. [PubMed: 18508075]
10. Chakravarthy S, Sternberg SH, Kellenberger CA, Doudna JA. Substrate-specific kinetics of Dicer-catalyzed RNA processing. J Mol Biol. 2010; 404:392–402. [PubMed: 20932845]
11. Lee HY, Doudna JA. TRBP alters human precursor microRNA processing in vitro. RNA. 2012; 18:2012–9. [PubMed: 23006623]
12. Noland CL, Ma E, Doudna JA. siRNA repositioning for guide strand selection by human Dicer complexes. Mol Cell. 2011; 43:110–21. [PubMed: 21726814]
13. Gregory RI, Chendrimada TP, Cooch N, Shiekhattar R. Human RISC couples microRNA biogenesis and posttranscriptional gene silencing. Cell. 2005; 123:631–40. [PubMed: 16271387]
14. Welker NC, et al. Dicer's helicase domain discriminates dsRNA termini to promote an altered reaction mode. Mol Cell. 2011; 41:589–99. [PubMed: 21362554]
15. Tsutsumi A, Kawamata T, Izumi N, Seitz H, Tomari Y. Recognition of the pre-miRNA structure by Drosophila Dicer-1. Nat Struct Mol Biol. 2011; 18:1153–8. [PubMed: 21926993]
16. Ma E, Zhou K, Kidwell MA, Doudna JA. Coordinated activities of human dicer domains in regulatory RNA processing. J Mol Biol. 2012; 422:466–76. [PubMed: 22727743]
17. Lau PW, Potter CS, Carragher B, MacRae IJ. Structure of the human Dicer-TRBP complex by electron microscopy. Structure. 2009; 17:1326–32. [PubMed: 19836333]
18. Wang HW, et al. Structural insights into RNA processing by the human RISC-loading complex. Nat Struct Mol Biol. 2009; 16:1148–53. [PubMed: 19820710]
19. Lau PW, et al. The molecular architecture of human Dicer. Nat Struct Mol Biol. 2012; 19:436–40. [PubMed: 22426548]
20. Danev R, Nagayama K. Transmission electron microscopy with Zernike phase plate. Ultramicroscopy. 2001; 88:243–52. [PubMed: 11545320]
21. Danev R, Nagayama K. Single particle analysis based on Zernike phase contrast transmission electron microscopy. J Struct Biol. 2008; 161:211–8. [PubMed: 18082423]
22. Shigematsu H, Sokabe T, Danev R, Tominaga M, Nagayama K. A 3.5-nm structure of rat TRPV4 cation channel revealed by Zernike phase-contrast cryoelectron microscopy. J Biol Chem. 2010; 285:11210–8. [PubMed: 20044482]
23. Shimada A, et al. Curved EFC/F-BAR-domain dimers are joined end to end into a filament for membrane invagination in endocytosis. Cell. 2007; 129:761–72. [PubMed: 17512409]

24. Yamaguchi M, Danev R, Nishiyama K, Sugawara K, Nagayama K. Zernike phase contrast electron microscopy of ice-embedded influenza A virus. J Struct Biol. 2008; 162:271–6. [PubMed: 18313941]
25. Murata K, et al. Zernike phase contrast cryo-electron microscopy and tomography for structure determination at nanometer and subnanometer resolutions. Structure. 2010; 18:903–12. [PubMed: 20696391]
26. Haase AD, et al. TRBP, a regulator of cellular PKR and HIV-1 virus expression, interacts with Dicer and functions in RNA silencing. EMBO Rep. 2005; 6:961–7. [PubMed: 16142218]
27. Danev R, Glaeser RM, Nagayama K. Practical factors affecting the performance of a thin-film phase plate for transmission electron microscopy. Ultramicroscopy. 2009; 109:312–25. [PubMed: 19157711]
28. MacRae IJ, Doudna JA. An unusual case of pseudo-merohedral twinning in orthorhombic crystals of Dicer. Acta Crystallogr D Biol Crystallogr. 2007; 63:993–9. [PubMed: 17704568]
29. Kelley LA, Sternberg MJ. Protein structure prediction on the Web: a case study using the Phyre server. Nat Protoc. 2009; 4:363–71. [PubMed: 19247286]
30. Luo D, et al. Structural insights into RNA recognition by RIG-I. Cell. 2011; 147:409–22. [PubMed: 22000018]
31. Scheres SH, et al. Disentangling conformational states of macromolecules in 3D-EM through likelihood optimization. Nat Methods. 2007; 4:27–9. [PubMed: 17179934]
32. Roberts AJ, et al. AAA+ Ring and linker swing mechanism in the dynein motor. Cell. 2009; 136:485–95. [PubMed: 19203583]
33. Cianfrocco MA, et al. Human TFIID Binds to Core Promoter DNA in a Reorganized Structural State. Cell. 2013; 152:120–31. [PubMed: 23332750]
34. MacRae IJ, Ma E, Zhou M, Robinson CV, Doudna JA. In vitro reconstitution of the human RISC-loading complex. Proc Natl Acad Sci U S A. 2008; 105:512–7. [PubMed: 18178619]
35. Giraldez AJ, et al. Zebrafish MiR-430 promotes deadenylation and clearance of maternal mRNAs. Science. 2006; 312:75–9. [PubMed: 16484454]
36. Daniels SM, et al. Characterization of the TRBP domain required for dicer interaction and function in RNA interference. BMC Mol Biol. 2009; 10:38. [PubMed: 19422693]
37. Radermacher M, Wagenknecht T, Verschoor A, Frank J. Three-dimensional reconstruction from a single-exposure, random conical tilt series applied to the 50S ribosomal subunit of Escherichia coli. J Microsc. 1987; 146:113–36. [PubMed: 3302267]
38. Kim DH, et al. Synthetic dsRNA Dicer substrates enhance RNAi potency and efficacy. Nat Biotechnol. 2005; 23:222–6. [PubMed: 15619617]
39. Nam Y, Chen C, Gregory RI, Chou JJ, Sliz P. Molecular basis for interaction of let-7 microRNAs with Lin28. Cell. 2011; 147:1080–91. [PubMed: 22078496]
40. Michlewski G, Cáceres JF. Antagonistic role of hnRNP A1 and KSRP in the regulation of let-7a biogenesis. Nat Struct Mol Biol. 2010; 17:1011–8. [PubMed: 20639884]
41. Mayr F, Schütz A, Döge N, Heinemann U. The Lin28 cold-shock domain remodels pre-let-7 microRNA. Nucleic Acids Res. 2012; 40:7492–506. [PubMed: 22570413]
42. Gu S, et al. The loop position of shRNAs and pre-miRNAs is critical for the accuracy of dicer processing in vivo. Cell. 2012; 151:900–11. [PubMed: 23141545]
43. Cenik ES, et al. Phosphate and R2D2 restrict the substrate specificity of Dicer-2, an ATP-driven ribonuclease. Mol Cell. 2011; 42:172–84. [PubMed: 21419681]
44. Zhang H, Kolb FA, Brondani V, Billy E, Filipowicz W. Human Dicer preferentially cleaves dsRNAs at their termini without a requirement for ATP. EMBO J. 2002; 21:5875–85. [PubMed: 12411505]
45. Cifuentes D, et al. A novel miRNA processing pathway independent of Dicer requires Argonaute2 catalytic activity. Science. 2010; 328:1694–8. [PubMed: 20448148]
46. Cheloufi S, Dos Santos CO, Chong MM, Hannon GJ. A Dicer-independent miRNA biogenesis pathway that requires Ago catalysis. Nature. 2010; 465:584–9. [PubMed: 20424607]
47. Ludtke SJ, Baldwin PR, Chiu W. EMAN: semiautomated software for high-resolution single-particle reconstructions. J Struct Biol. 1999; 128:82–97. [PubMed: 10600563]

48. van Heel M, Harauz G, Orlova EV, Schmidt R, Schatz M. A new generation of the IMAGIC image processing system. J Struct Biol. 1996; 116:17–24. [PubMed: 8742718]
49. Hosokawa F, Danev R, Arai Y, Nagayama K. Transfer doublet and an elaborated phase plate holder for 120 kV electron-phase microscope. J Electron Microsc (Tokyo). 2005; 54:317–24. [PubMed: 16123062]
50. Frank J, et al. SPIDER and WEB: processing and visualization of images in 3D electron microscopy and related fields. J Struct Biol. 1996; 116:190–9. [PubMed: 8742743]
51. Scheres SH, Núñez-Ramírez R, Sorzano CO, Carazo JM, Marabini R. Image processing for electron microscopy single-particle analysis using XMIPP. Nat Protoc. 2008; 3:977–90. [PubMed: 18536645]
52. Tang G, et al. EMAN2: an extensible image processing suite for electron microscopy. J Struct Biol. 2007; 157:38–46. [PubMed: 16859925]
53. Hohn M, et al. SPARX, a new environment for Cryo-EM image processing. J Struct Biol. 2007; 157:47–55. [PubMed: 16931051]
54. Wiedenheft B, et al. Structures of the RNA-guided surveillance complex from a bacterial immune system. Nature. 2011; 477:486–9. [PubMed: 21938068]
55. Ogura T, Iwasaki K, Sato C. Topology representing network enables highly accurate classification of protein images taken by cryo electron-microscope without masking. J Struct Biol. 2003; 143:185–200. [PubMed: 14572474]
56. Voss NR, et al. A toolbox for ab initio 3-D reconstructions in single-particle electron microscopy. J Struct Biol. 2010; 169:389–98. [PubMed: 20018246]
57. Lander GC, et al. Appion: an integrated, database-driven pipeline to facilitate EM image processing. J Struct Biol. 2009; 166:95–102. [PubMed: 19263523]
58. Voss NR, Yoshioka CK, Radermacher M, Potter CS, Carragher B. DoG Picker and TiltPicker: software tools to facilitate particle selection in single particle electron microscopy. J Struct Biol. 2009; 166:205–13. [PubMed: 19374019]
59. Scheres SH, et al. Maximum-likelihood multi-reference refinement for electron microscopy images. J Mol Biol. 2005; 348:139–49. [PubMed: 15808859]

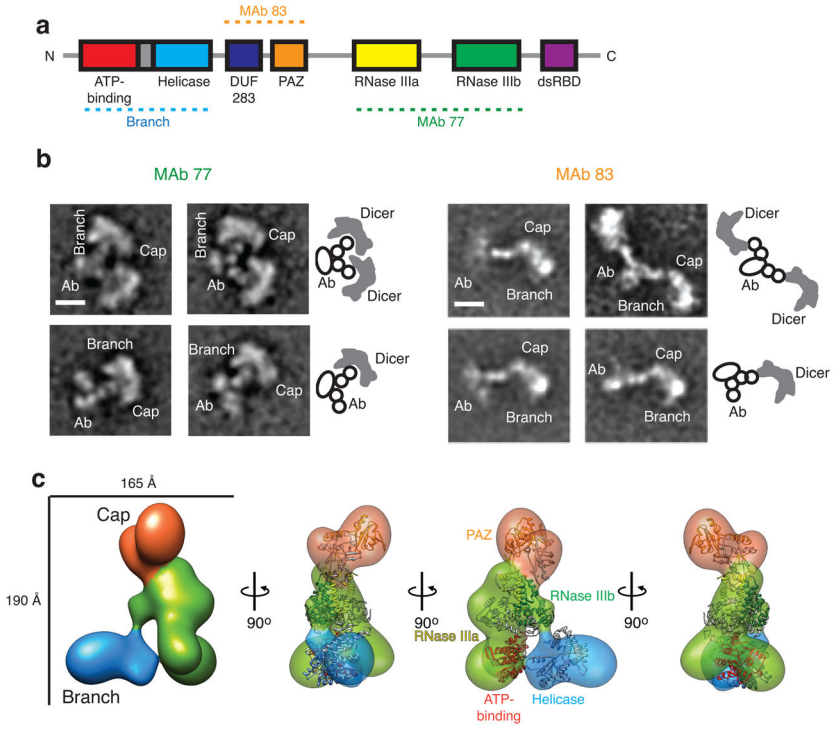

Figure 1. Domain architecture and cryo-EM structure of human Dicer

(**a**) Domain organization of human Dicer and color code used for labeling regions of the EM map (dashed lines) and docked atomic structures (solid boxes). (**b**) Reference-free 2D class averages of negatively stained human Dicer in complex with antibody mAb 77 (left) and mAb 83 (right)[26], along with cartoon representations. The cap and branch of individual Dicer molecules are labeled. Scale bars represent 100 Å. (**c**) Cryo-EM reconstruction of human Dicer. Regions labeled by antibodies in (**b**) and the DExH/D domain assigned in our previous work[18] are segmented and colored on the EM density: mAb 83-labeled region (orange), mAb 77-labled region (green), DExH/D domain (light blue). Crystal structures of homologous domains have been docked into the map based on the antibody localization and segmentation and are color coded and labeled as in (**a**): RNase IIIa (yellow), RNase IIIb (green), and PAZ domain (orange), from *Giardia intestinalis* Dicer (PDB 2QVW[28]); ATP-binding (red) and helicase (light blue) domains of a homology model of Dicer's helicase based on human RIG-I (PDB 2YKG[30]). The cap and branch of the enzyme are labeled based on our previous nomenclature[18].

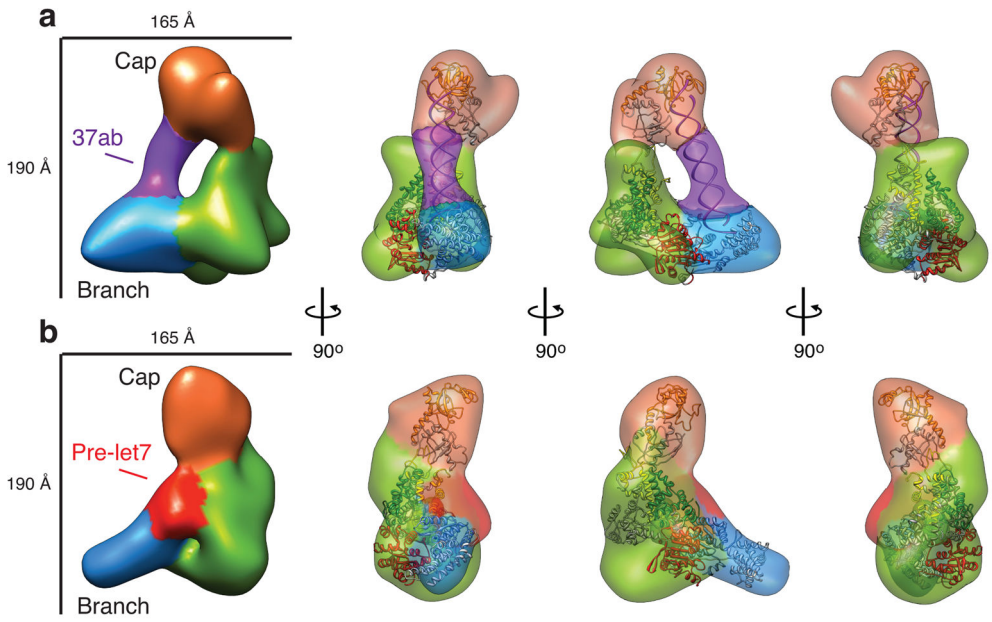

Figure 2. A pre-siRNA spans human Dicer between the cap and branch, while a pre-miRNA binds the platform of the enzyme

(**a**,**b**) Cryo-EM reconstructions of human Dicer–37ab (**a**) and human Dicer–pre-let7 (**b**) at ~29 Å and ~31 Å resolution, respectively. Segmented regions of the EM density and atomic structures are colored as in Fig. 1. The pre-siRNA, 37ab, is modeled as a 35-bp A-form RNA duplex within its segmented density colored purple (**a**). The pre-miRNA, pre-let7, is not modeled and the segmented density is colored red (**b**).

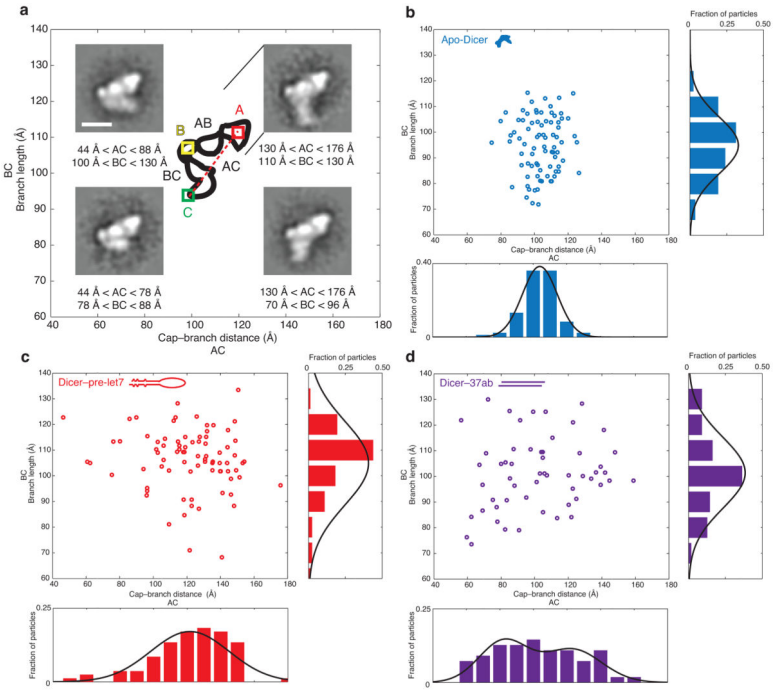

Figure 3. RNA substrates induce structural rearrangements in human Dicer

(**a**) Class averages corresponding to specific ranges of cap–branch distances (AC) and branch lengths (BC), mapped onto the graph used for plotting the raw data from negatively stained apo-Dicer and Dicer–RNA complexes. Scale bar indicates 100 Å. The inset shows a schematic of how domain positions and distance measurements were calculated. (**b–d**) Distribution of branch length (BC) vs. cap–branch distance (AC) for apo-Dicer (**b**), Dicer–pre-let7 (**c**), and Dicer–37ab (**d**) complexes, marked with open light blue, red, and purple circles, respectively. Normalized histograms of the distance distribution and Gaussian approximations are shown along each axis following the same coloring scheme.

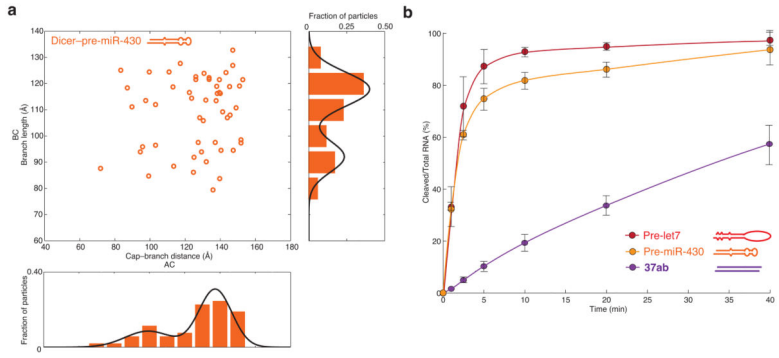

Figure 4. A domain reorganization of human Dicer in response to pre-miRNAs correlates with increased dicing efficiency

(**a**) Distribution of branch length (BC) vs. cap–branch distance (AC) for negatively stained Dicer–pre-miR-430 complexes, marked with open orange circles. Normalized histograms of the distance distribution and Gaussian approximations are shown along each axis. (**b**) Cleavage activity (cleaved/total RNA %) vs. time of human Dicer on 37ab, pre-miR-430, and pre-let7. Error bars indicate the standard deviation from six independent experiments for 37ab and pre-let7 and three independent experiments for pre-miR-430, respectively.

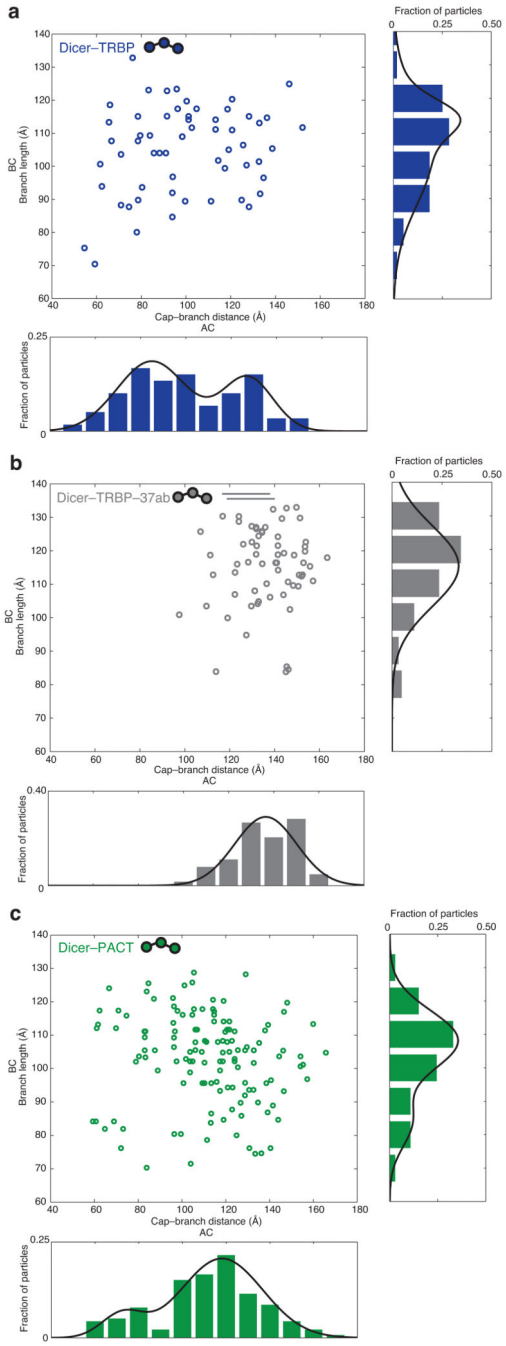

Figure 5. dsRBPs promote conformational sampling of human Dicer for dsRNA substrate-loading

(**a–c**) Distribution of branch length (BC) vs. cap–branch distance (AC) for negatively stained Dicer–TRBP (**a**), Dicer–TRBP–37ab (**b**), and Dicer–PACT (**c**) complexes marked with open dark blue, grey, and green circles, respectively. Normalized histograms of the distance distribution and Gaussian approximations are shown along each axis following the same coloring scheme.

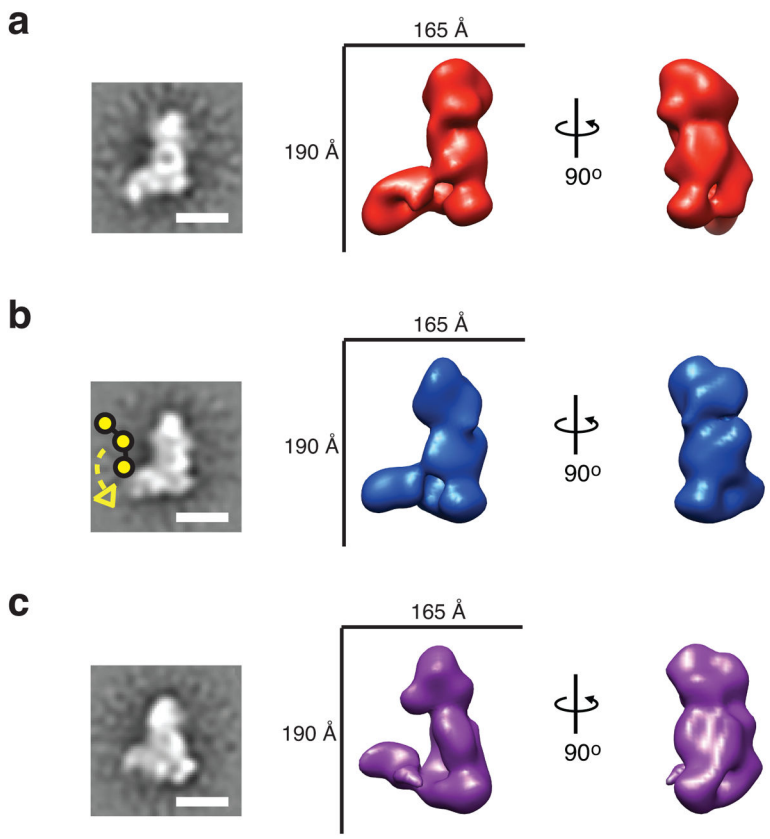

Figure 6. 3D reconstructions of major Dicer conformers show that branch position affects accessibility to the platform

(**a–c**) Reference-free 2D class averages used for RCT (**left**) and the final 3D conformers of the enzyme captured by multi-model refinement **(right**) of negatively stained Dicer–PACT particles against the three RCT models, showing the open (**a**), canonical (**b**), and closed (**c**) state of the enzyme in red, blue, and purple, respectively. The models are colored to reflect the similarity observed to conformations of Dicer–RNA complexes based on correlation with reference-free 2D class averages of unique subpopulations of Dicer–pre-let7 (red), apo-Dicer (light blue), and Dicer–37ab (purple) as shown in Fig. 3. Scale bar for 2D class averages corresponds to 100 Å. PACT is illustrated as a string of three yellow spheres with a flexible linker connecting it to the DExH/D domain in (b) based on our previous single particle analysis of Dicer–TRBP[18]. The yellow arrow denotes its predicted range of motion.

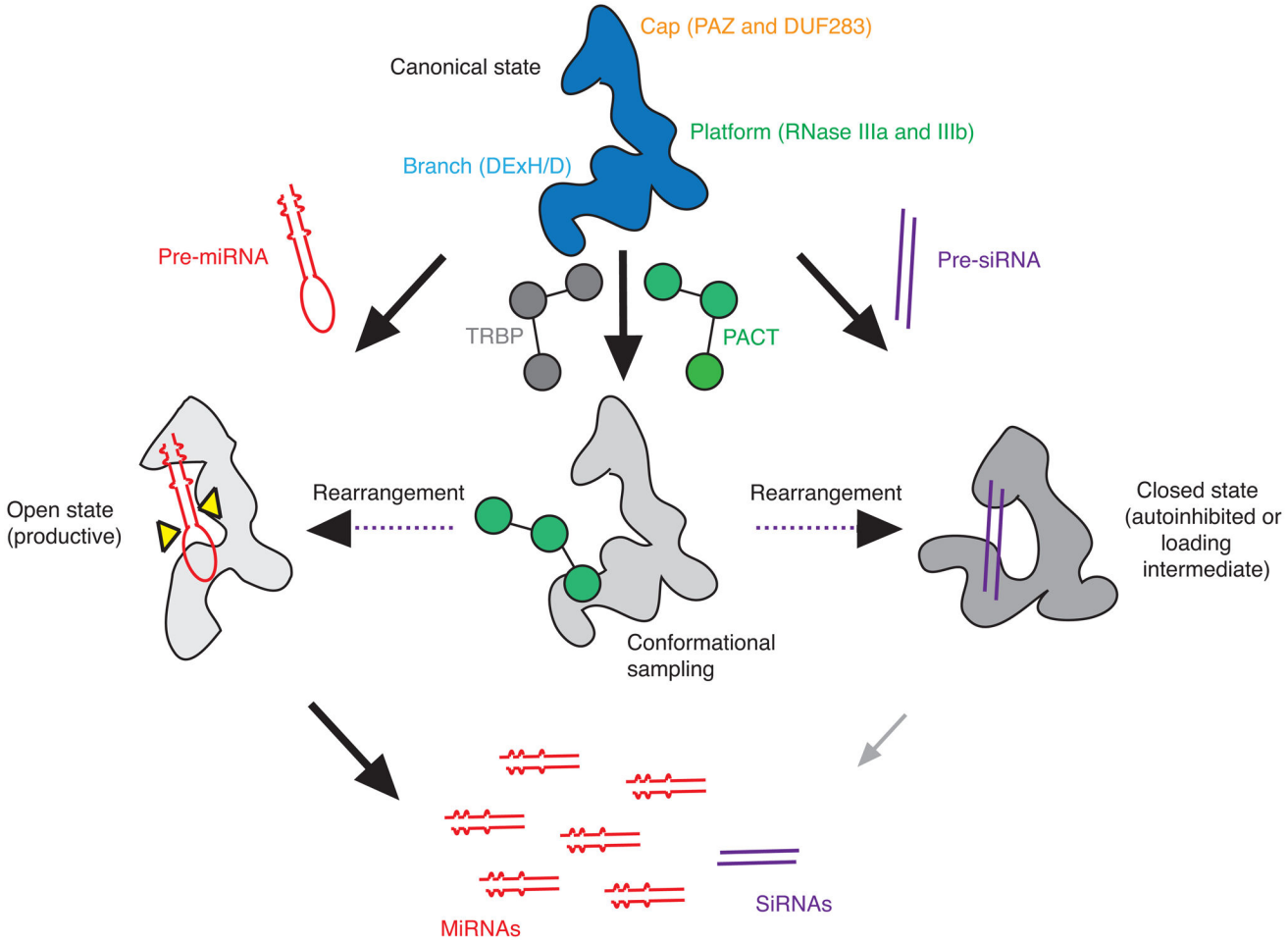

Figure 7. Model for small RNA processing by human Dicer

RNA-binding by the helicase domain of human Dicer causes rearrangement of the enzyme in a substrate-specific manner. Binding of a pre-miRNA occurs along the platform and is accompanied by an outward bending of the helicase domain away from the platform, while pre-siRNAs are trapped between the PAZ and helicase domain away from the catalytic sites. dsRBPs may poise the enzyme for recognition of RNA precursors and/or productive loading of the enzyme. Dicer was drawn by tracing the contour of a class average from each state, respectively.

Table 1

Quantities of Dicer particles in each conformation for negatively stained apo-Dicer and Dicer–RNA or cofactor complexes (in %).

	Open (cap–branch > 120 Å)	Canonical (cap–branch = 86–120 Å)	Closed (cap–branch ≤ 85 Å)
apo-Dicer	2	95	3
Dicer–pre-let7	46	45	9
Dicer–37ab	27	33	40
Dicer–pre-miR-430	70	24	6
Dicer–TRBP	25	45	30
Dicer–TRBP–37ab	85	15	0
Dicer–PACT	35	49	16